PNAS RESEARCH ARTICLE | PLANT BIOLOGY OPEN ACCESS

Structure of ATP synthase from an early photosynthetic bacterium *Chloroflexus aurantiacus*

Xin Zhang[a,b], Jingyi Wu[a,b], Zhenzhen Min[a], Jiamao Wang[a], Xin Hong[a,b], Xinkai Pei[a], Zihe Rao[c], and Xiaoling Xu[a,b,1]

Affiliations are included on p. 10.

Edited by Donald Ort, University of Illinois at Urbana Champaign, Urbana, IL; received December 10, 2024; accepted January 28, 2025

F-type ATP synthase (F_1F_O) catalyzes proton motive force-driven ATP synthesis in mitochondria, chloroplasts, and bacteria. Different from the mitochondrial and bacterial enzymes, F_1F_O from photosynthetic organisms have evolved diverse structural and mechanistic details to adapt to the light-dependent reactions. Although complete structure of chloroplast F_1F_O has been reported, no high-resolution structure of an F_1F_O from photosynthetic bacteria has been available. Here, we report cryo-EM structures of an intact and functionally competent F_1F_O from *Chloroflexus aurantiacus* (*Ca*F_1F_O), a filamentous anoxygenic phototrophic bacterium from the earliest branch of photosynthetic organisms. The structures of *Ca*F_1F_O in its ADP-free and ADP-bound forms for three rotational states reveal a previously unrecognized architecture of ATP synthases. A pair of peripheral stalks connect to the *Ca*F_1 head through a dimer of δ-subunits, and associate with two membrane-embedded a-subunits that are asymmetrically positioned outside and clamp *Ca*F_O's c_{10}-ring. The two a-subunits constitute two proton inlets on the periplasmic side and two proton outlets on the cytoplasmic side, endowing *Ca*F_1F_O with unique proton translocation pathways that allow more protons being translocated relative to single a-subunit F_1F_O. Our findings deepen understanding of the architecture and proton translocation mechanisms of F_1F_O synthases and suggest innovative strategies for modulating their activities by altering the number of a-subunit.

ATP synthase | proton translocation | photosynthesis | photosynthetic bacteria

F-type ATP synthase (F_1F_O) catalyzes the proton motive force (PMF)-driven ATP synthesis at the final step of oxidative phosphorylation and photophosphorylation in mitochondria (mtF_1F_O), chloroplasts (cF_1F_O), and bacteria (bF_1F_O) (1–3). These enzymes comprise a soluble F_1 (Fraction 1) that synthesizes ATP and a membrane-embedded F_O (Oligomycin-binding fraction) that translocates protons (H^+) across the membrane. F_1 is composed of a hexamer of three asymmetric heterodimers ($\alpha_3\beta_3$) (4), and a central stalk (comprising the γ- and ε-subunits in bacteria) that rotates inside $\alpha_3\beta_3$ and attaches to a c-ring to form the "rotor" (5). F_O consists of the c-ring of 8 to 17 c-subunits, and an a-subunit that forms two aqueous half-channels to conduct proton translocation (6). The F_1 and F_O a-subunit are connected by a single peripheral stalk on one side, forming the "stator" of the enzyme (7). The peripheral stalk comprises δ and two b-subunits in most bF_1F_O. While cF_1F_O and F_1F_O from some photosynthetic bacteria, such as cyanobacteria and purple non-sulfur bacteria, have two nonidentical but related subunits b and b′ (8–14). The peripheral stalk composition of mtF_1F_O is more substantial, comprising OSCP (homologous to δ-subunit), b, d, F6, f, i/j, and 8 subunits (15, 16). During ATP synthesis, PMF–driven rotation of the c-ring is transmitted by the central stalk to induce sequential conformational changes in $\alpha_3\beta_3$, where the catalytic sites alternate from being empty to being occupied by Mg-ADP and phosphate (Pi), which are further condensed to Mg-ATP (4). The proton translocation activity of F_O is thus coupled to the ATP synthesis in F_1, forming an efficient molecular turbine employing rotary catalysis for energy conversion (3, 17).

F_1F_O synthases from photosynthetic organisms or organelles have modified the c- and γ-subunits to adapt the rapid PMF changes resulting from light fluctuations and light-dependent bioenergetic demands (6, 8). The c-ring stoichiometry determines the number of protons required for a full rotation of the rotor (3). Therefore, the bioenergetic cost of synthesizing a single ATP molecule can be evaluated by the H^+-to-ATP ratio, which equals the number of c-subunits (n) divided by the number of ATP molecules (three) synthesized per full rotation (18). Relative to bF_1F_O and mtF_1F_O having c-ring stoichiometries ranging from 8 to 13 (19–24), plant and cyanobacterial F_1F_O synthases have larger c-ring stoichiometries vary between 13 and 15 (8, 25), generating higher H^+-to-ATP ratios that are favored to maintain the PMF in a range where ATP synthesis is supported but photodamage is minimized (6, 26, 27). In response to light intensity and light/dark

Significance

F-type ATP synthase (F_1F_O) catalyzes proton motive force-driven ATP synthesis in mitochondria, chloroplasts, and bacteria. We have identified an architecture of F_1F_O from *Chloroflexus aurantiacus* (*Ca*F_1F_O), a bacterium from the earliest branch of photosynthetic organisms. Different from previously described ATP synthases, *Ca*F_1F_O has two peripheral stalks and two proton-conducting a-subunits, which constitute two proton inlets and two proton outlets, endowing *Ca*F_1F_O with unique proton translocation pathways that allow more protons (presumably double of the single a-subunit) to translocate across the membrane within a single cycle of ATP synthesis. Our findings provide structural insights into the proton translocation mechanism of ATP synthases from photosynthetic bacteria and suggest innovative strategies to modulate the function of F_1F_O synthases.

Author contributions: X.Z. and X.X. designed research; X.Z., J. Wu, Z.M., J. Wang, X.H., and X.P. performed research; X.Z. and X.X. analyzed data; and X.Z., Z.R., and X.X. wrote the paper.

The authors declare no competing interest.

This article is a PNAS Direct Submission.

[1] To whom correspondence may be addressed. Email: xuxl@hznu.edu.cn.

This article contains supporting information online at https://www.pnas.org/lookup/suppl/doi:10.1073/pnas.2425824122/-/DCSupplemental.

transitions, cF_1F_O regulates its activity through redox regulation of a disulfide bond formed in a ~40 amino acid insertion of the γ-subunit (8, 28). Cyanobacterial F_1F_O contains an insertion in the γ-subunit but lacks redox regulation (29), indicating diversified regulatory mechanisms for the photosynthetic F_1F_O synthases. Given their central roles in light-driven ATP production, these F_1F_O synthases are viewed as attractive targets for modulating photosynthesis and photoconversion efficiencies in engineered plants, synthetic organelles, or light-driven biomimetic systems (27, 30–32).

The complete structure of cF_1F_O from spinach has been resolved at high resolution, providing significant insights into the structural and mechanistic details of photosynthetic F_1F_O from higher plants. Although the crystal structure of the γ-ε complex from photosynthetic cyanobacterium *Thermosynechococcus elongatus* has been reported, high-resolution structure of an intact photosynthetic F_1F_O from photosynthetic bacteria is needed to deepen our understanding of the architecture and catalytic mechanism of F_1F_O from the early photosynthetic organisms. *Chloroflexus aurantiacus* (*C. aurantiacus*) is a representative bacterium of *Chloroflexi*, a phylum of green filamentous anoxygenic phototrophs (FAPs) that are evolved earlier than cyanobacteria and other anoxygenic phototrophs, thus forming the earliest branch of bacteria capable of photosynthesis (*SI Appendix*, Fig. S1) (33, 34). Different from plants, algae, and cyanobacteria, *C. aurantiacus* employs anoxygenic photosynthesis through a unique light-dependent electron transport chain, which ultimately releases electrons and protons into the periplasm to generate the PMF required for ATP synthesis, comprises a peripheral antenna chlorosome, light-harvesting (LH)-reaction center (RC) complexes (35, 36), an alternative complex III (ACIII) (37, 38) and a blue-copper protein auracyanin (Ac) (39) that functionally replace the cytochrome b_6f complex and plastocyanin (PC) in oxygenic phototrophs (40, 41) (Fig. 1*A*).

Here, we isolated an intact and functionally competent F_1F_O from *C. aurantiacus* (*Ca*F_1F_O) and determined structures of *Ca*F_1F_O in its ADP-free and ADP-bound forms for three rotational states. Different from any of the previously described ATP synthases, *Ca*F_1F_O contains two peripheral stalks and two membrane-embedded a-subunits that collectively constitute two proton inlet half-channels on the periplasmic side and two proton outlet half-channels on the cytoplasmic side, endowing *Ca*F_1F_O with unique proton translocation pathways.

Results

Overall Structure of *Ca*F_1F_O. We isolated *Ca*F_1F_O from phototrophically grown *C. aurantiacus* J-10-fl cells using a modification of previous methods (42). Blue native polyacrylamide gel electrophoresis (PAGE) of *Ca*F_1F_O showed a single band with a molecular weight near 669 kDa, and tricine–sodium dodecyl sulfate (SDS)-PAGE revealed

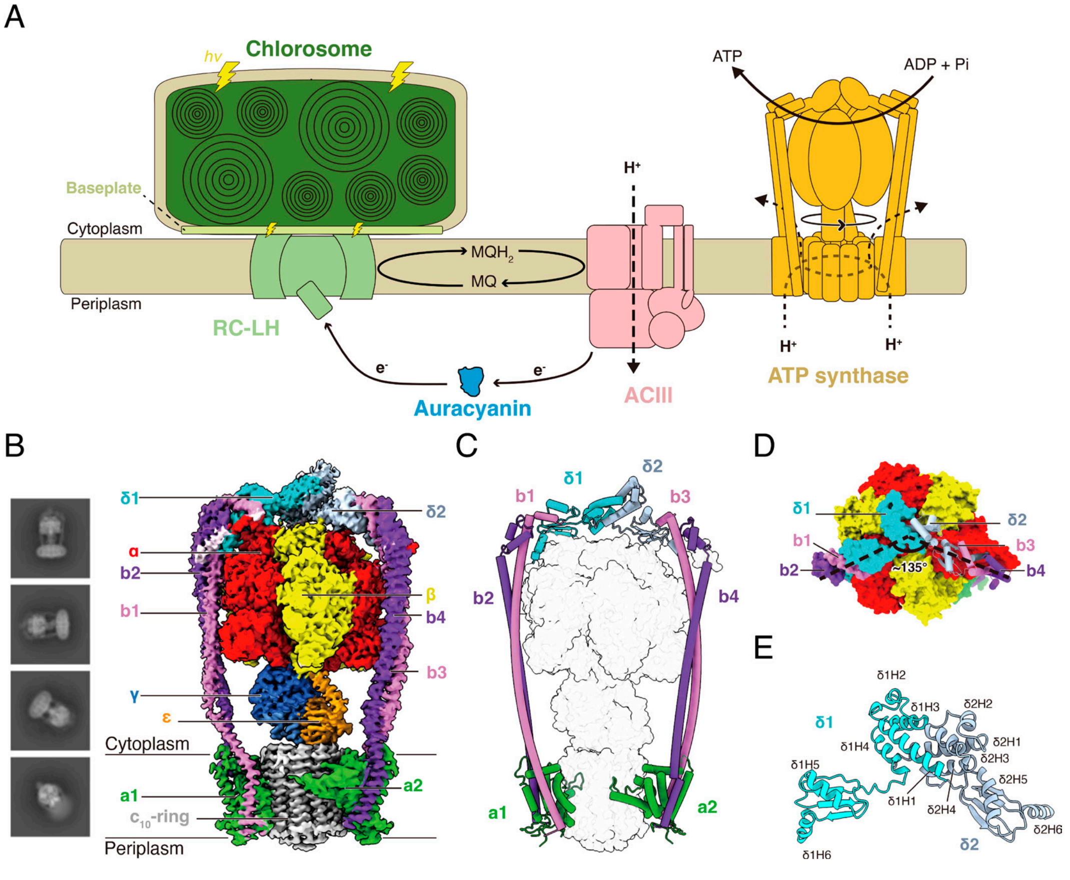

Fig. 1. Overall structure of *Chloroflexus aurantiacus* ATP synthase (*Ca*F_1F_O). (*A*) Diagram illustrating the photophosphorylation process of *C. aurantiacus*. The light-dependent electron transport chain (ETC), which ultimately releases electrons and protons (H^+) into the periplasm to generate the PMF required for ATP synthesis, comprises a peripheral antenna chlorosome, light-harvesting (LH)-reaction center (RC) complexes, an alternative complex III (ACIII), and a blue-copper protein auracyanin (Ac). (*B*) 2D class averages and side view of the cryo-EM maps of *Ca*F_1F_O at rotational State 1. The overall structure comprises *Ca*F_1 ($\alpha_3\beta_3\gamma\varepsilon$) and membrane-embedded *Ca*F_O (a_2c_{10}) connected by two peripheral stalks ($b_4\delta_2$). (*C*) The atomic model highlights two a-subunits (a1 and a2) and two peripheral stalks (b1b2δ1 and b3b4δ2). (*D*) Top view of the *Ca*F_1 interactions with two peripheral stalks, separated by ~135° (dashed black line); the δ1-C and δ2-C domains connect the b1-subunit and the b3-subunit to the *Ca*F_1 head. (*E*) Dimer of the δ-subunits. Each δ-subunit comprises two domains separated by a flexible hinge. The N-terminal domain (δ-N) is a bundle of four α helices (δH1 to δH4); the C-terminal domain (δ-C) is a four-stranded β sheet with two α helices (δH5 to δH6). Two δ-Ns are interlocked at the δH1 and δH3 helices to form a dimer. Subunit color code: α, Red; β, Yellow; δ1, Cyan; δ2, Steel blue; γ, Blue; ε, Orange; b1 and b3, Orchid; b2 and b4, Dark orchid; a, Forest green; c, Silver.

eight bands with molecular weights ranging from ~10 to 70 kDa (*SI Appendix*, Fig. S2 *A* and *B*). Peptide mass fingerprinting (PMF) showed eight *Ca*F$_1$F$_O$ subunits (αβγεδabc); these are encoded by a gene cluster (*Caur*_3040-3047) (*SI Appendix*, Table S1). When reconstituting the isolated complex into proteoliposomes, *Ca*F$_1$F$_O$ was fully active in synthesizing ATP, but it was autoinhibited in ATP hydrolysis (*SI Appendix*, Fig. S2 *C* and *D*).

Single particle cryo-EM analysis of the isolated *Ca*F$_1$F$_O$ generated three 3D maps, each with the rotor arrested in a different rotary state (named rotational States 1, 2, and 3) (*SI Appendix*, Figs. S2*E* and S3 *A* and *B*). These three maps were reconstructed and refined to overall resolutions of 2.84, 2.89, and 3.31 Å, respectively (*SI Appendix*, Fig. S3 *A*–*D*). Focused refinement of each state improved the local resolutions of the *Ca*F$_O$ regions to 3.16, 3.30, and 3.98 Å, and the local resolutions of the two peripheral stalks to 3.48, 3.85, and 4.60 Å (*SI Appendix*, Fig. S3*E* and Table S2). No nucleotide densities were observed in any of the three β-subunits, while all three α-subunits were resolved with bound ATP molecules (*SI Appendix*, Fig. S2*F*). We therefore refer to these cryo-EM structures as "ADP-free *Ca*F$_1$F$_O$."

We subsequently incubated *Ca*F$_1$F$_O$ with Mg-ADP and successfully obtained the "ADP-bound" β-subunits in the *Ca*F$_1$F$_O$ structures for three rotational states at 2.89, 2.96, and 3.18 Å resolutions (*SI Appendix*, Fig. S4 *A*–*D*); further focused refinement improved the resolutions to 3.97, 4.10, and 4.28 Å for the *Ca*F$_O$ region and 4.08, 4.95, and 5.18 Å for the peripheral stalks in each rotational state (*SI Appendix*, Fig. S4*E* and Table S3). These cryo-EM maps enabled the building of accurate atomic models for the α-, β-, γ-, ε-, a-, b-, c-subunits, and the C-terminal domain of δ-subunit (named δ-C) in both the ADP-free and ADP-bound structures (*SI Appendix*, Figs. S5 and S6). The N-terminal domain of the δ-subunit (δ-N) was resolved in the rotational State 1, while it appeared at lower resolution and was not modeled in States 2 or 3 (Fig. 1*B* and *SI Appendix*, Fig. S2*E*).

F$_1$F$_O$ synthases contain a single peripheral stalk that exclusively connects the catalytic head ($\alpha_3\beta_3$) and a membrane-embedded a-subunit on one side of the c-ring. Distinct from all ATP synthase/ATPase structures reported to date, *Ca*F$_1$F$_O$ consists of a *Ca*F$_1$ head ($\alpha_3\beta_3$) and a membrane-embedded *Ca*F$_O$ (a_2c_{10}) that are connected by two peripheral stalks (δ_2b_4) and a central stalk (γε), giving rise to a subunit stoichiometry of $\alpha_3\beta_3\gamma\varepsilon\delta_2a_2b_4c_{10}$ (Fig. 1 *B* and *C*). On top of the *Ca*F$_1$ head, a homodimer of two δ-subunits connects the b1- and b3-subunits to the $\alpha_3\beta_3$ hexamer at two positions (separated by ~135°) (Fig. 1*D*). Within the *Ca*F$_O$ region, the coiled coils of the peripheral stalks b1b2 and b3b4 each bifurcate and anchor one copy of a-subunit, forming the stator of the enzyme (Fig. 1 *B* and *C*). The central stalk (γε) inserts into the *Ca*F$_1$ head and attaches to the c$_{10}$-ring as the rotor. This architecture of *Ca*F$_1$F$_O$ with two peripheral stalks and two a-subunits is also distinct from *Tt*V$_1$V$_O$ (43), which contains two peripheral stalks but has a single a-subunit (*SI Appendix*, Fig. S7).

Conformational Plasticity of the Stalks. The three rotational states of *Ca*F$_1$F$_O$ are differentiated by rotation of the central stalk and c$_{10}$-ring at ~120°, 125°, and 114° (Fig. 2*A* and *SI Appendix*, Fig. S8 and Movie S1). Rotation of the central stalk induces sequential conformational changes in the *Ca*F$_1$ head and forces it to tilt from the *Ca*F$_O$ symmetry axes, a process known as "precession"(8, 43). The precession angles between the *Ca*F$_1$ and *Ca*F$_O$ symmetry axes are measured at 2.2°, 0.3°, and 0.8° for three rotational states (*SI Appendix*, Fig. S2*E*). Relative to the two a-subunits, the c-subunit positions are offset at ~9.3° for rotational State 2 relative to States 1 and 3 (*SI Appendix*, Fig. S8*C*). This is similar to cF$_1$F$_O$, in which the rotor shows unequal rotation of ~103°, 112°, and 145° at three rotational states, and there is a ~10° offset of the c-subunits (8). Superposition of the central stalks in the three rotational states gives RMSD values of 0.392 (between States 1 and 2), 0.558 (between States 2 and 3), and 0.731 (between State 3 and 1), indicating structural rigidity of the γ- and ε- subunits (Fig. 2*B*). The central stalk rigidity resembles that in bF$_1$F$_O$ and cF$_1$F$_O$ (8, 21, 44). It is distinct from *Tt*V$_1$V$_O$ (which also has two peripheral stalks) (43) and mtF$_1$F$_O$ (45), in which considerable flexibility occurs at the central stalk during rotation of the c-ring.

Different from any of the previously reported F$_1$F$_O$, *Ca*F$_1$F$_O$ contains a dimer of two δ-subunits that connects two peripheral stalks to the *Ca*F$_1$ head (Fig. 2*C* and *SI Appendix*, Fig. S7). Each δ-subunit comprises two domains separated by a flexible hinge. The δ-N domain (Met1-Arg85) consists of a bundle of four α helices, it shares no structural similarity to any previously reported δ-N structures (Fig. 1*E* and *SI Appendix*, Fig. S9*A*). Two δ-N domains are interlocked at δH1 and δH3 helices, forming a dimer that sits in a central position on top of the *Ca*F$_1$ head (Fig. 2*D*). The positions of the δ-N dimer shift by ~16 Å, ~2 Å, and ~14 Å during the transitions from the State 1 to 2, from the State 2 to 3, and from the State 3 to 1 (Fig. 2*E*), respectively. These analyses indicate that the δ-N dimer contributes to coordinate the conformational changes that occur during *Ca*F$_1$ precession.

Similar to previously reported F$_1$F$_O$, the δ-C domain (Arg85-Ser157) contains a four-stranded β-sheet and two α helices (δH5 and δH6) (Fig. 1*E* and *SI Appendix*, Fig. S9*A*). The β-sheet of each δ-C interacts with the N-terminal β-barrel of the α-subunits (α1-N and α2-N) through extensive hydrogen bonding interactions (Fig. 2*D* and *SI Appendix*, Fig. S9*B*). The δH5 and δH6 helices of δ1-C and δ2-C separately accommodate the kinked C-terminus of the b1- and b3-subunits (Fig. 2*D*). During the transitions among three rotational states, the α-Ns are twisted in different directions but maintaining contact with the two δ-Cs, in which only δ2-C confers minimal conformational changes (Fig. 2*F* and *SI Appendix*, Fig. S9 *C* and *D*).

In the middle coiled-coil regions of the peripheral stalks, b1b2-subunits are bent into distinct curvatures (without contacting the adjacent αβ heterodimers); yet for all three rotational states, b3b4-subunits are in close contact with the α-subunits by salt bridges between amino acids pairs αGlu485-b3Arg85 and αGlu514-b3Arg73 (Fig. 2*F*). Among the three rotational states, no conformational changes occur at the membrane regions of the peripheral stalks that anchor the a-subunits (Fig. 2*C*). These findings indicate that the two peripheral stalks have conformational plasticities at the top δ-subunit dimer and the middle coiled-coil regions during transition among the three rotational states. Compared to the single peripheral stalk in cF$_1$F$_O$ and bF$_1$F$_O$ synthases, the two peripheral stalks provide considerable structural stability and conformational flexibility for coupling *Ca*F$_1$ precession to c$_{10}$-ring rotation in *Ca*F$_O$. As the *Ca*F$_O$ torsional force is transmitted by the central stalk to *Ca*F$_1$ catalytic sites, the middle coiled-coil regions of the two peripheral stalks each bend in distinct curvatures, which prevent wobbling of the *Ca*F$_1$ head and thus distribute energy minima between the rotary states. Ultimately, the dimer comprising two δ-subunits twists on top of the *Ca*F$_1$ head, helping to release the elastic energy stored in the bent peripheral stalks.

Mg-ADP Induced Conformational Change in *Ca*F$_1$ and ε-Inhibition. According to Boyer's binding change mechanism for ATP synthesis and the structural studies of bovine mitochondria F$_1$, the three catalytic β-subunits adopt different conformations in sequential order from binding ADP and Pi (β_{DP}), producing tightly bound ATP (β_{TP}) to release of ATP (β_E) (4, 46). Similar

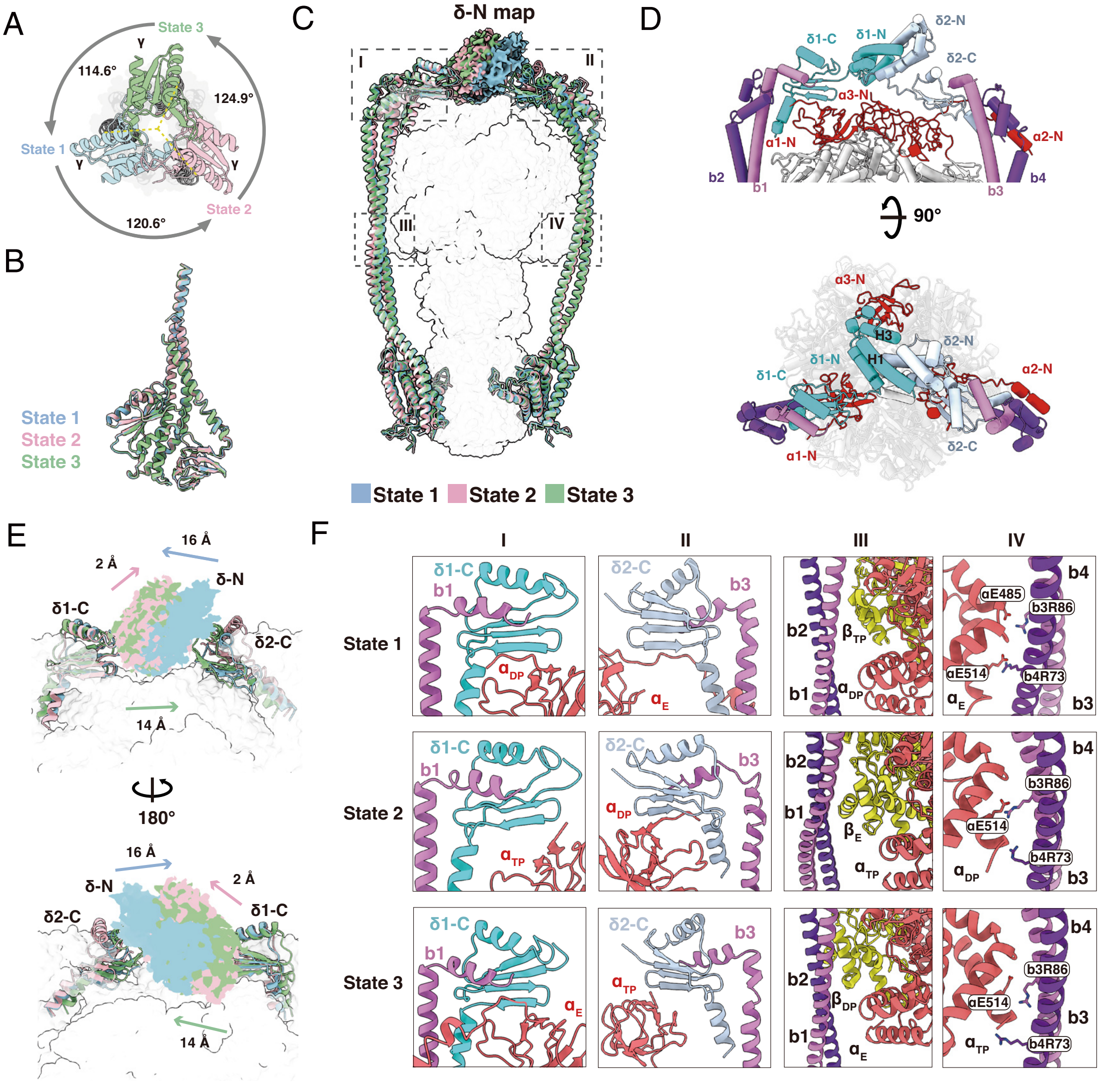

Fig. 2. Conformational flexibility of the stalks among three rotary states of *Ca*F$_1$F$_O$. (*A*) *Top* view (from *Ca*F$_1$ to *Ca*F$_O$) of the central stalk (represented by the γ-subunit) and the c$_{10}$-ring (represented by the c1-subunit) in rotational State 1 (light blue), State 2 (light pink), and State 3 (light green). In State 2, the central stalk is rotated by 120.6° relative to State 1; in State 3, the central stalk is rotated by 124.9° relative to State 2. The rotation angle from State 3 back to State 1 is 114.6°. (*B*) Superposition of the central stalk (γε) in three rotational states. (*C*) Superposition of the two peripheral stalks aligned on the a1- and a2-subunits in three rotational states. Conformational changes of the *Top* and *Middle* coiled-coil regions that contact the *Ca*F$_1$ head are highlighted by dashed boxes and are labeled with roman numbers I–IV. (*D*) Side, and *Top* views of the interactions between two peripheral stalks (b1b2δ1 and b3b4δ2) and the *Ca*F$_1$ head (α$_3$β$_3$). (*E*) Conformational changes of the δ-N dimer among three rotational states. The positions of the δ-N dimer are shifted by ~16 Å, ~2 Å, and ~14 Å during the transitions from State 1 to 2, from State 2 to 3, and from State 3 to 1, while the δ2-C confers minimal conformational changes. (*F*) Close-up views of the conformational changes of two peripheral stalks and the *Ca*F$_1$ head among three rotational states. The amino acid residues involved in forming hydrogen bonding interactions are shown as sticks.

to reported F$_1$F$_O$ synthases, *Ca*F$_1$ is composed of a hexamer of three conformationally different αβ heterodimers around a central stalk (Fig. 3*A*). Each α- and β-subunit comprises an N-terminal β-barrel domain, a central nucleotide-binding domain, and a C-terminal helical domain (*SI Appendix*, Fig. S10*A*). Compared to β-subunit, each α-subunit contains an additional N-terminal helix (N-helix) (*SI Appendix*, Fig. S10*A*). The N-helix is resolved in only one of the three α-subunits; it interacts with b3b4-subunits through hydrophobic interactions, preventing random movement of this peripheral stalk (Fig. 3*A* and *SI Appendix*, Fig. S10 *B* and *C*). In each rotational state of the ADP-free and ADP-bound structures, three α-subunits adopt identical conformations, in which the nucleotide-binding sites are occupied with Mg-ATP (Fig. 3 *A* and *B* and *SI Appendix*, Figs. S2*F* and S10*D*). The three catalytic β-subunits do not contain any nucleotides in the ADP-free structures, adopt "open" (β$_E$, empty), "closed" (β$_{TP}$, Mg-ADP bound), and "open" (β$_{DP}$, Mg-ADP, and Pi bound) conformations similar to those observed in our ADP-bound structures (Fig. 3 *A* and *B*). The nucleotide-binding sites of *Ca*F$_1$F$_O$ are highly conserved among F$_1$F$_O$ synthases from bacteria to eukaryotes (Fig. 3*B* and *SI Appendix*, Fig. S11).

Superposition of the State 1 ADP-free and ADP-bound *Ca*F$_1$F$_O$ structures gives a main chain RMSD value of 0.399 Å, indicating that ADP binding does not obviously affect the *Ca*F$_1$F$_O$ conformation (Fig. 3*A*). Upon ADP binding, the C-terminal helical domains (helices H12-18) of β$_E$, β$_{DP}$, and α$_{DP}$, especially helix15 (H15) of β$_{DP}$ and β$_E$ shift to positions close to the nucleotide-binding pocket (Fig. 3*C* and *SI Appendix*, Fig. S12*A*), implicating these regions in coordination of nucleotide binding. In the ADP-bound structure, the H15 helices in β$_{DP}$ and β$_{TP}$ are positioned close to the nucleotide-binding pocket (Fig. 3*D* and *SI Appendix*, Fig. S12*B*). These findings support that ADP binding induces conformational changes in α$_3$β$_3$ that effect ATP synthesis, with especially pronounced changes for the H15 helices in catalytic β-subunits.

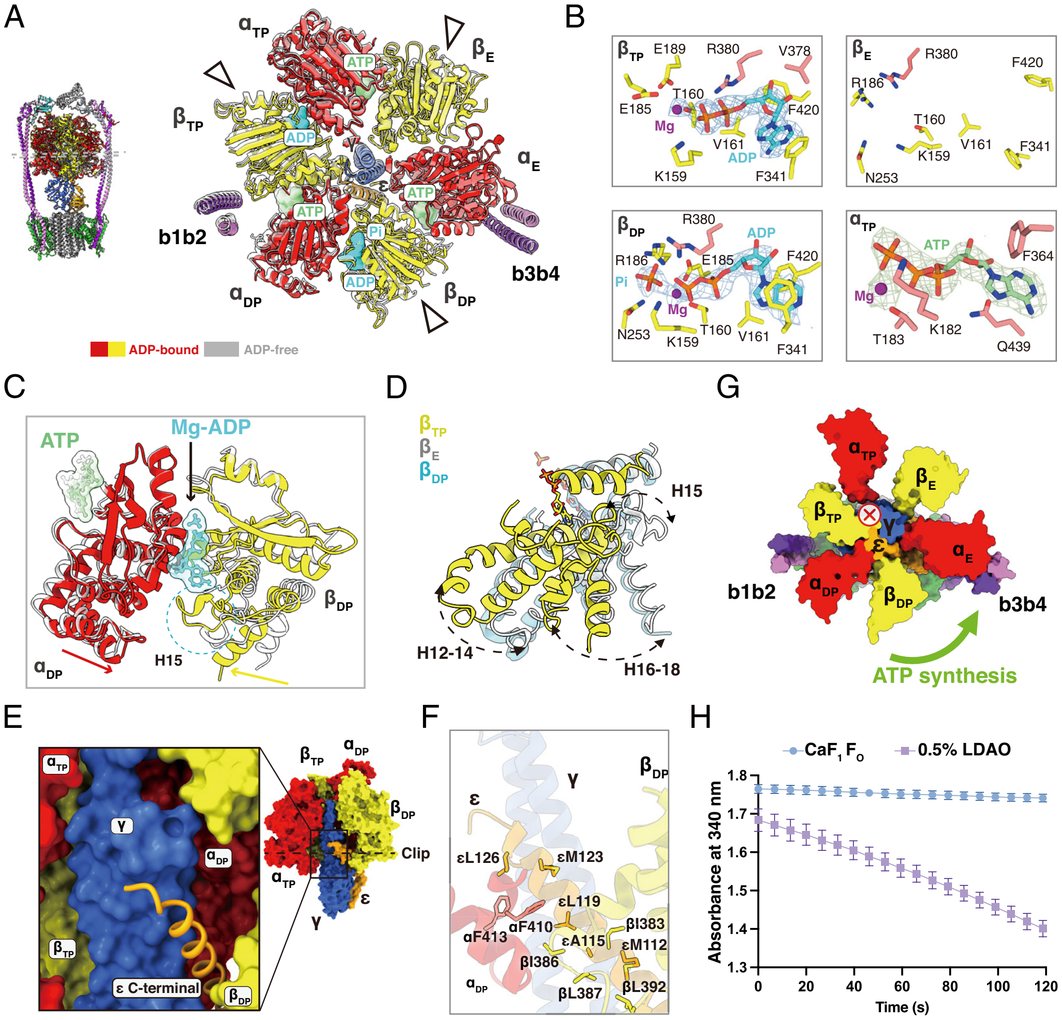

Fig. 3. The *Ca*F_1 structure and autoinhibition by the ε-subunit. (*A*) Cross-section through the nucleotide-binding domains of ADP-bound (colored) and ADP-free (white) *Ca*F_1 heads. Each αβ heterodimer is stalled in different conformations ($\alpha_E\beta_E$, $\alpha_{DP}\beta_{DP}$, $\alpha_{TP}\beta_{TP}$) of the binding change mechanism. The catalytic β-subunits conferring conformational changes upon ADP-binding are indicated with hollow arrows. The central and peripheral stalks are shown to present their interactions with the *Ca*F_1 head. (*B*) Close-up views of the nucleotide-binding pockets in the catalytic β-subunits and noncatalytic α-subunit. The β_{TP} site contains ADP (cyan) and Mg (purple); the β_{DP} site contains ADP, Pi (cyan), and Mg (purple); β_E is empty. α_{TP} contains one ATP (green) and one Mg (purple). (*C*) Superposition of the $\alpha_{DP}\beta_{DP}$ heterodimers in the ADP-bound (colored) and ADP-free (white) *Ca*F_1F_O, showing the conformational changes (red and yellow arrows) of the C-terminal helical domains (H12-18). ATP (green) and Mg-ADP (cyan) are shown as sticks (fitted into the cryo-EM densities). (*D*) Side views of the aligned β_{TP} (yellow), β_{DP} (turquoise), and β_E (gray) in the ADP-bound *Ca*F_1F_O, revealing substantial relocation (black dashed arrows) of C-terminal helical domains (H12-18). (*E*) Structure of the *Ca*F_1 in a surface representation, revealing insertion of εCTD into the *Ca*F_1 head. (*F*) Close-up views of the εCTD and α_{DP}/β_{DP} interactions. Amino acid residues involved in forming hydrophobic interactions are shown as sticks. (*G*) Cross-section of the *Ca*F_1 head along the dashed line in panel (*E*). Steric clashes between the ε-subunit (orange) and β_{TP} block rotation of the rotor in the direction of ATP hydrolysis but allow its free rotation for ATP synthesis (green arrow). (*H*) *Ca*F_1F_O shows residual ATP hydrolysis activity, which is stimulated by adding 0.5% (v/v) lauryldimethylamine oxide (LDAO).

Previous studies have reported that the bF_1F_O from *Escherichia coli* (*E. coli*) (44, 47–49), *Bacillus PS3* (21), and *Acinetobacter baumannii* (*A. baumannii*) (50) avoid wasteful ATP hydrolysis by employing an extended C-terminal helix in the ε-subunit (εCTD), which forms a single helix and maintains an "up conformation" to inhibit ATP hydrolysis. Analogous to these enzymes, the ADP-free and ADP-bound *Ca*F_1F_O both contain an extended εCTD, which protrudes into the α_{DP} and β_{DP} interface and extends along the γ-subunit to reach the central rotor cavity (Fig. 3*E* and *SI Appendix*, Fig. S12 *B*–*F*). The inserted εCTD forms extensive hydrophobic interactions with α_{DP} and β_{DP}, forcing β_{DP} to adopt an open conformation (Fig. 3*F* and *SI Appendix*, Fig. S12 *B* and *E*). Insertion of the εCTD therefore physically blocks the clockwise rotation of γ-subunit (i.e., for ATP hydrolysis), but it is still free to turn counterclockwise for ATP synthesis (Fig. 3*G*). During one complete central stalk rotation, upon Mg-ADP and Pi binding, β_E transitions to the β_{DP} and then to β_{TP}, producing one ATP molecule that is ultimately released when the closed β_{TP} reverts to open β_E (*SI Appendix*, Fig. S10*E*). This scenario is consistent with our enzymatic analyses of *Ca*F_1F_O showing autoinhibition of ATP hydrolysis activity and its stimulation by lauryldimethylamine oxide (LDAO) (Fig. 3*H*), a compound previously used to disable the ε-inhibition in *E. coli* F_1F_O (48).

***Ca*F_O Contains Two Membrane-Embedded a-Subunits and One c_{10}-ring.** All proton-translocating ATP synthases/ATPases described to date contain a single a-subunit, which lies outside the c-ring and conducts transmembrane proton translocation to power its rotation (8, 16, 19–21, 28, 44, 45, 47–59). Exceptionally, *Ca*F_1F_O contains two instances of membrane-embedded a-subunits, which asymmetrically surround and clamp a c_{10}-ring by interacting with two peripheral stalks on both sides (Fig. 4*A* and *SI Appendix*, Fig. S13*A*). Each a-subunit of *Ca*F_1F_O has a fold of six α-helices (aH1-H6) that also occurs in chloroplasts (8), yeast (52), and other bacterial F_1F_O (20, 21, 44) (*SI Appendix*, Fig. S13 *B* and *C*). Both aH1 and aH2 span across the membrane and insert into the space between two peripheral b-subunits (Fig. 4*A* and *SI Appendix*, Fig. S13*A*). aH3-aH4 and aH5-aH6 helices form two long membrane-intrinsic hairpins, in which aH3-aH4 hairpin is in close contact with the peripheral stalks through extensive hydrophobic interactions, and aH5-aH6 hairpin constitutes the interface with the c_{10}-ring (Fig. 4*A*).

Compared to the a-subunits from *E. coli* (44), *Bacillus PS3* (21), *A. baumannii* (50), *Mycobacterium smegmatis* (*M. smegmatis*) (20), *Spinacia oleracea* (*S. oleracea*) (8), *and Saccharomyces cerevisiae* (*S. cerevisiae*) (52) F_1F_O synthases, *C. aurantiacus* a-subunit has a unique insertion sequence (His142-Thr172) within the aH3-aH4 linker (Pro127-Pro187) (Fig. 4 *B* and *C* and *SI Appendix*, Fig. S14). Superposition of the *Ca*F_1F_O a-subunit with that from *E. coli*, *Bacillus PS3*, *S. cerevisiae*, and *S. oleracea* F_1F_O indicate obvious structural similarity at the aH3-aH4 hairpin, while also revealing a substantially longer aH3 and aH4 linker in *Ca*F_1F_O that is partially disordered from His136 to Pro157 (Fig. 4*C*). Again, unique to *Ca*F_1F_O, there is a Cys135-Cys173 disulfide bond that connects the aH3 and aH4 helices immediately in front of the disordered region, making the aH3-aH4 hairpin in *Ca*F_1F_O adopt a similar conformation to those known for a-subunits of *E. coli*, *Bacillus PS3*, and *S. oleracea* (Fig. 4 *B* and *C*). We found that exposure of *Ca*F_1F_O to dithiothreitol (DTT) did not affect its integrity (blue native gel assay) or ATP synthesis activity (Fig. 4*D* and *SI Appendix*, Fig. S15*A*). The localization of the Cys135-Cys173 disulfide bond on the periplasmic surface of *Ca*F_1F_O makes it distinct from the disulfide bond that has been observed in the γ-subunit of cF_1F_O, which employs redox regulation to avoid wasteful ATP hydrolysis in the dark (2, 8, 28, 61).

Each *Ca*F_1F_O c-subunit resembles those in cF_1F_O and bF_1F_O, comprising a hairpin of two transmembrane α-helices, which are

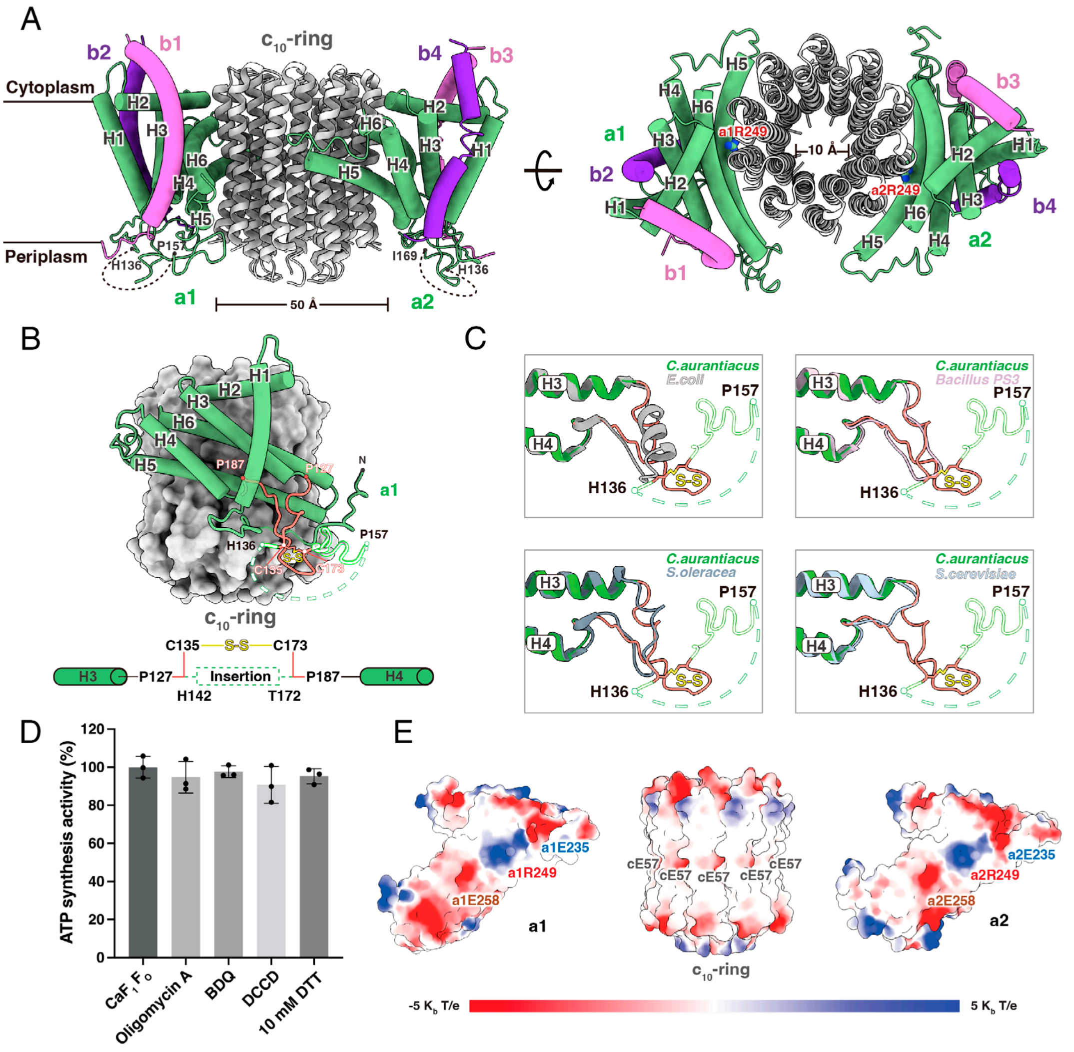

Fig. 4. Two a-subunits in *Ca*F_O. (*A*) Side (*Left*) and top (*Right*) views of *Ca*F_O, comprising two a-subunits (a1 and a2 in forest green) that lie outside and clamp a ~50 Å diameter c_{10}-ring (gray). Two peripheral stalks (b1/b3 in orchid, and b2/b4 in dark orchid) each bifurcate and anchor one copy of the a-subunit. The disordered regions in the a1-subunit (His136-Pro157) and a2-subunit (His136-Ile169) are indicated by dashed lines. The aArg249 checkpoints are shown as sticks. (*B*) Spatial organization for the Cys135-Cys173 disulfide bond and a-subunit insertion (His142-Thr172). Six conserved helices of the a1-subunit are shown as cylinders. The positions of the amino acid residues Pro127 and Pro187 in the aH3-aH4 linker and His136 and Pro157 in the disordered region are indicated with dots; the Cys135-Cys173 disulfide bond is shown as sticks. (*C*) Superposition of the *Ca*F_1F_O a-subunit with those from *Escherichia coli* (PDB: 6OQW, gray), *Bacillus PS3* (PDB: 6N2Y, pink), *Spinacia oleracea* (PDB: 6FKF, steel blue), and *Saccharomyces cerevisiae* (PDB: 6CP6, light blue), indicating the structural conservation of the aH3-aH4 hairpins; the *Ca*F_1F_O a-subunit has a substantially longer aH3-aH4 linker (partially disordered from His136 to Pro157). The Cys135-Cys173 disulfide bond immediately connects the aH3 and aH4 helices in front of the disordered region. (*D*) ATP synthesis activity of *Ca*F_1F_O in 10 mM DTT, inhibitors oligomycin A, bedaquiline (BDQ), and dicyclohexylcarbodiimide (DCCD), respectively. Each bar represents the mean from n = 3 separate assays, with errors are represented as SD from the mean. (*E*) Surface electrostatic potentials of the a1-subunit (*Left*), c_{10}-ring (*Center*), and a2-subunit (*Right*). The proton inlet (centered on E258) and outlet (centered on E235) half-channels in each a-subunit contain extensive negative charges. The positively, negatively, and neutrally charged residues on the surface are indicated with blue, red, and white, respectively. The surface electrostatic potential was calculated with the electrostatics plugin in ChimeraX (60) with the scale shown in units of K_b T/e.

connected by a loop that electrostatically attaches to the central stalk to guide its rotation (*SI Appendix*, Fig. S15 *B* and *C*). Strictly conserved Glu57 residues from each c-subunit are exposed on the outer membrane helix, forming a ring of negative charges on the exterior surface of the c_{10}-ring (Fig. 4*E*). The two *Ca*F_1F_O a-subunits cover most of the exterior surface, leaving only three of the ten c-subunits completely exposed (Fig. 4*B*). Relative to a single a-subunit, the presence of two a-subunits increases the a/c_{10}-ring interface area (e.g., 7,021 $Å^2$ versus 2,825 $Å^2$ of *E. coli* F_1F_O; *SI Appendix*, Fig. S15*D*). The two a-subunits also apparently "mask" the binding site for inhibitors that target the a/c-ring interface or the c-ring glutamates or aspartates (20, 56, 57, 62–64). Notably, such masking is supported by our enzymatic analyses, in which *Ca*F_1F_O ATP synthesis activity was not affected by inhibitors known to target the c-ring glutamates [e.g., oligomycin A, bedaquiline (BDQ), and dicyclohexylcarbodiimide (DCCD)] (Fig. 4*D*). Thus, beyond revealing *Ca*F_1F_O's unique architecture comprising two membrane-embedded a-subunits and one c_{10}-ring, these results suggest that *Ca*F_1F_O's expanded a/c_{10}-ring interface area can plausibly explain the previously reported inability of multiple compounds to inhibit the ATP synthases.

Proton Translocation Pathway in *Ca*F_1F_O. Previous studies have established that the a-subunit forms two half-channels (inlet and outlet) to and from the conserved glutamates or aspartates in the c-ring for proton translocation (8, 16, 19, 21, 44, 45, 48, 51–55, 58). The two half-channels are spatially and electrostatically separated by a strictly conserved arginine residue, which serves as "checkpoint" to prevent proton leakage from the inlet to the outlet half-channels (43, 54). In *Ca*F_1F_O structure, we calculated the solvent-accessible regions of *Ca*F_O interior and identified four half-channels comprising aqueous cavities at the interface between two a-subunits and the c_{10}-ring (Fig. 5*A*). Each a-subunit contains two half-channels, both constitute negatively charged patches on the cytoplasmic (centered at aGlu235) and periplasmic sides (centered at aGlu258), which are separated by a patch of positive charge from a highly conserved aArg249 in the middle (Fig. 4*E*). The positive charge compensates with the negative charges of cGlu57 residues in the middle of the c_{10}-ring (Fig. 4*E*), ensuring that cGlu57 residues release protons before encountering the two checkpoints a1Arg249 and a2Arg249. The arrangement of two half-channels in each *Ca*F_1F_O a-subunit resembles those observed in previously reported ATP synthases/ATPases. One distinction is the presence of the two a-subunits that form two inlet half-channels (inlet1 and inlet2) on the periplasmic side and two outlet half-channels (outlet1 and outlet2) on the cytoplasmic side separated with two Arg249 checkpoints (Fig. 5*A* and *SI Appendix*, Fig. S16*A*).

The structure of dimeric ATP synthase from bovine mitochondria provides evidence that the proton uptake from the mitochondrial matrix proceeds via a Grotthus chain of water molecules, suggested by the unmodeled density in the inlet half-channel (55). In *Ca*F_1F_O, no clear cryo-EM densities of water molecules have been observed in any of the four half-channels. The dimension of the "L-shaped" inlet half-channel is ~7 Å at the narrowest position, providing enough space for freely passing of the water molecules (*SI Appendix*, Fig. S16 *B* and *C*). In each a-subunit, the inlet half-channel begins from periplasmic aHis170 and aAsp171, and then passes through a tunnel formed by aHis31, aSer131, aGlu258, aGlu280 from the extended aH3 and aH4 linker and the U-turn half of the aH5-H6 hairpin. These proton-carrying residues are positioned with edge-to-edge distances of more than ~4.6 Å (*SI Appendix*, Fig. S16 *D* and *E*), which are adequate for accommodating water molecules to conduct the proton transfer via a Grotthus mechanism. The inlet half-channel ends at aAsn253, which can deliver proton to the nearby cGlu57 residue for protonation (Fig. 5*B* and *SI Appendix*, Fig. S16 *B*–*E*).

The outlet is delineated by an aqueous cavity composed of hydrophilic residues at the interface between the cytoplasmic half of the aH5-H6 hairpin and the c_{10}-ring, starting from the adjacent cGlu57 that receives proton, passing aSer238, aLys242, aGlu239 to aGlu235, and ending at aLys220 on the cytoplasmic side (Fig. 5*B* and *SI Appendix*, Fig. S16 *B*–*E*). These residues are positioned with edge-to-edge distances of more than ~4.0 Å, except aGlu239 and aLys242 that forms a weak hydrogen bond (3.4 Å) (*SI Appendix*, Fig. S16 *D*–*E*), indicating the protons in the outlet half-channel could also be transferred via a Grotthus mechanism. Superposition of the two a-subunits revealed similar sidechain orientations of the amino acid residues that constitute the proton inlet and outlet half-channels (Fig. 5*B*).

The edge-to-edge distance of the inlet and outlet half-channels in each a-subunit is ~13Å, which matches the space between adjacent cGlu57 residues on the c_{10}-ring (Fig. 5 *C* and *D*). This distance matching allows simultaneous protonation of one cGlu57 and deprotonation of its adjacent cGlu57. Superposition of the ten c-subunits in rotational State 1 revealed distinct sidechain orientations of the cGlu57 residues (*SI Appendix*, Fig. S15*E*) and indicated that the protonated and deprotonated cGlu57 residues adopt different sidechain conformations during rotation. Specifically, at the interface of the c_{10}-ring and aH5-aH6 hairpin, c1Glu57 (numbered in the ATP synthesis direction) directs its carboxylate against the guanidine group of a1Arg249 (3.1 Å), forming a salt bridge that releases the proton and transiently arrests movement of the c1Glu57 carboxylate (Fig. 5*C*). On the other side, the protonated c5Glu57 carboxyl inserts against the outlet 2 and releases the proton, while the carboxylate of c6Glu57 stretches along the c_{10}-ring and rotates past the a2Arg249 checkpoint (Fig. 5 *C* and *D*).

These structural analyses reveal a putative proton translocation pathway in *Ca*F_1F_O. During ATP synthesis, the presence of the two proton inlets (inlet1 and inlet2) allows protons to travel toward the negatively charged cGlu57 carboxylates at the a/c_{10}-ring interfaces. Once being protonated, driven by PMF, the neutralized cGlu57 carboxyl partitions into the lipid phase and makes one counterclockwise rotary substep [a full rotation of the c_{10}-ring comprises ten rotary substeps (51)]. Each rotary substep brings the adjacent cGlu57 into the a/c_{10}-ring interface for protonation, thus initiating subsequent rotary substeps. Upon encountering the a1Arg249 and a2Arg249 checkpoints, the cGlu57 residues release protons into the nearest outlets, where protons are translocated to the cytoplasm with higher pH. The cGlu57 residues mediate proton translocation for both inlets: protons from inlet1 are released to outlet2 following four rotary substeps of the c_{10}-ring, while protons from inlet2 are released to the nearest outlet1 following six rotary substeps. Thus, the sequential protonation and deprotonation of the cGlu57 residues drive rotation of the c_{10}-ring. After passing the a1Arg249 and a2Arg249 checkpoints, the deprotonated cGlu57 residues receive protons as they successively enter the inlet1 and inlet2, starting a new cycle of transmembrane proton translocation (Fig. 5*E* and Movie S2).

Discussion

ATP synthases transform the energy inherent in the transmembrane electrochemical gradient into formation of a covalent phosphoanhydride bond stored in ATP. Here, based on structural analysis of *Ca*F_1F_O, we have revealed an architecture with the proton translocation pathway unique from any previously described ATP synthases. Two pairs of peripheral stalks connect

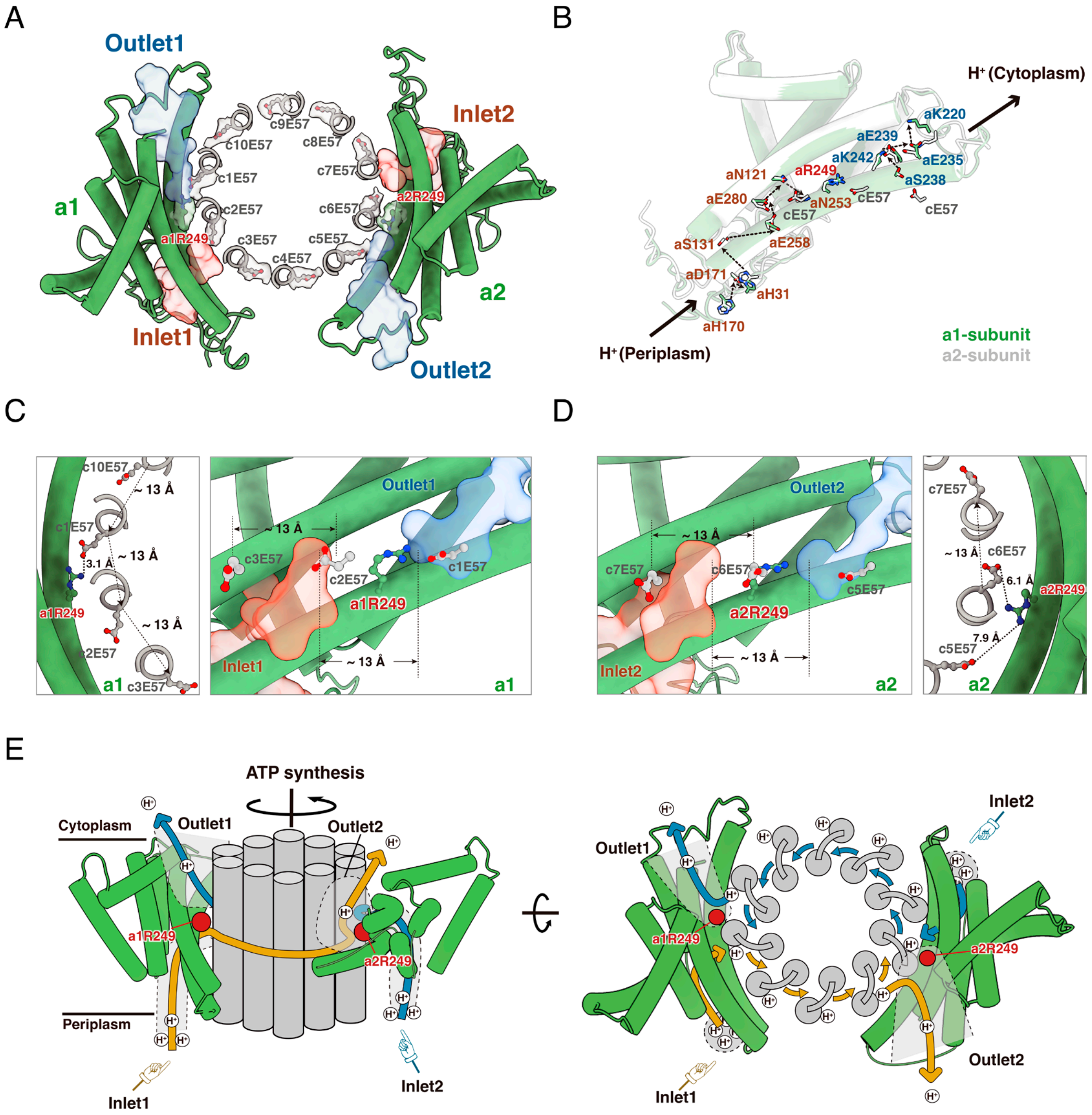

Fig. 5. Proton translocation in CaF_1F_O. (*A*) The *Top* view of a_2c_{10} features the proton inlet and outlet half-channels on the a1- and a2-subunits and the cGlu57 (silver sticks) conformations of the c_{10}-ring for rotational State 1. The long membrane-intrinsic hairpin of helices aH5 and aH6 follows the curvature of the c_{10}-ring, forming the periplasmic proton inlet half-channels (red transparent surface) and the cytoplasmic outlet half-channels (blue transparent surface). An aArg249 (green sticks) in each a-subunit separates the two half-channels and prevents proton leakage. The ten cGlu57 residues are shown as sticks (fitted into cryo-EM densities). (*B*) Superposition of the amino acid residues that constitute the proton translocating inlet (brown) and outlet (blue) half-channels of the a1-subunit (green) and a2-subunit (gray). (*C*) and (*D*) Edge-to-edge distances (black dashed lines) between the adjacent cGlu57 residues on the c_{10}-ring and their interactions with the aArg249 residues, and edge-to-edge distances (black arrows) between the inlet (red transparent surface) and outlet (blue transparent surface) half-channels in the a1-subunit (C) and a2-subunit (*D*). The hydrogen bond between cGlu57 and a1Arg249 is shown as a dashed line, with the distance labeled. (*E*) Proposed proton translocation pathway in CaF_1F_O. Driven by PMF, protons (black circles) from the periplasmic side enter the inlet1 and inlet2 half-channels (gray dash) and travel toward the negatively charged cGlu57 carboxylates at the a/c_{10}-ring interfaces. Upon protonation, the neutralized cGlu57 partitions into the lipid phase and makes one counterclockwise rotary substep (a full rotation of the c_{10}-ring comprises ten rotary substeps). Each rotary substep brings the adjacent cGlu57 into the a/c_{10}-ring interface for protonation, thus initiating subsequent rotary substeps. When encountering the a1Arg249 and a2Arg249 checkpoints (red dots), the cGlu57 residues release protons into the nearest outlet half-channels (gray dash), where protons are translocated to the cytoplasm with higher pH. Protons from inlet1 are released to outlet2 following four rotary substeps of the c_{10}-ring (orange arrow), while protons from inlet2 are released to the nearest outlet1 following six rotary substeps (blue arrow). After passing the a1Arg249 and a2Arg249 checkpoints, the deprotonated cGlu57 residues receive protons as they successively enter the inlet1 and inlet2, starting a new cycle of transmembrane proton translocation.

to the CaF_1 head through a dimer of two δ-subunits and associate with two membrane-embedded a-subunits in CaF_O. The two a-subunits constitute two proton inlet half-channels on the periplasmic side and two proton outlet half-channels on the cytoplasmic side, adding a second proton translocation pathway. Given the essential role of the a-subunit in conducting transmembrane proton translocation, our finding of CaF_1F_O's two a-subunits shakes up previous understanding about the structures and proton translocation mechanisms of ATP synthases.

Also distinct from previously described F_1F_O synthases, CaF_1F_O contains two peripheral stalks that are connected by a δ-N dimer. Prior to our study, the δ-N dimer has not been resolved in any of the reported F_1F_O structures. Multiple peripheral stalks have been observed in the TtV_1V_O (two) and V-ATPases (three) from human (65), rat brain (66), bovine brain (67), synaptic vesicles (68, 69), porcine kidney (70), yeast (71), and citrus fruit (72), but they are separately connected to the catalytic head via their C-terminal globular domains, leaving the space above the catalytic head unoccupied.

For F_1F_O synthases that contain a single peripheral stalk, the δ-N (cF_1F_O and bF_1F_O) or OSCP-N (mtF_1F_O) occupies the space above the pseudorotational symmetry axis of the F_1 head (*SI Appendix*, Fig. S7). At the same time as our studies, Ueno et al. have shown that the engineered *Bacillus PS3* F_1F_O can incorporate up to three peripheral stalks by deleting the δ-N and genetically fusing the δ-C to the N-terminal of α-subunit (73), indicating that the δ-N plays an important role in defining the number of peripheral stalks. Most likely, the δ-N structurally breaks the pseudothreefold symmetry of the F_1 head and limits the stoichiometry of the peripheral stalk to one (73).

To investigate the presence of the two peripheral stalks in CaF_1F_O from an evolutionary aspect, we constructed a phylogenetic tree based on the multiple sequence alignment of the δ-subunits from F_1F_O synthases. The phylogenetic analyses showed that the δ-subunits in F_1F_O synthases from the *Chloroflexi* phylum, such as *C. aurantiacus*, *Roseiflexus castenholzii*, and *Oscillochloris trichoides*, are classified into one group and conferring a close relationship (*SI Appendix*, Fig. S17 *A* and *B*). While the δ-subunits of *C. aurantiacus* and other photosynthetic bacteria (such as *Synechocystis* sp., *Rhodobacter capsulatus*, and *Heliobacterium modesticaldum*) are clustered in different groups and are evolved independently (*SI Appendix*, Fig. S17 *A* and *B*). Compared to previously reported bF_1F_O synthases, the bacterial species from *Chloroflexi* phylum all contain a shortened δ-N with ~20 amino acid sequences missing in the primary amino acid sequences (*SI Appendix*, Fig. S17*B*). Structural alignment further revealed the absence of α-helices in *C. aurantiacus* δ-N (*SI Appendix*, Fig. S17*C*), creating sufficient space to accommodate a δ-N dimer on top of the CaF_1 head. Given that deletion of the δ-N allows incorporation of up to three peripheral stalks in the engineered *Bacillus PS3* F_1F_O (73), the shortened δ-N most likely contributes to assembly of the two peripheral stalks in CaF_1F_O. Because the shortened δ-N is a common feature shared by the bacterial species from *Chloroflexi*, the presence of two peripheral stalks could be a specific feature of *Chloroflexi* F_1F_O synthases.

The most important functional significance of CaF_1F_O is the incorporation of two proton-conducting a-subunits accompanied with two peripheral stalks. Compared with F_1F_O synthases having a single a-subunit, it is notable that the two a-subunits in CaF_1F_O form two proton inlets and two proton outlets, allowing more protons (presumably double of the single a-subunit) to flow in-and-out the CaF_O during each cycle of ATP synthesis in CaF_1. As a result, CaF_1F_O is capable of translocating more protons from the periplasm to cytoplasm per ATP synthesized, yielding a higher H^+-to-ATP ratio relative to bF_1F_O synthases that also have a c_{10}-ring. This is supported by recent studies of the engineered *Bacillus PS3* F_1F_O, in which the enzyme containing three a-subunits showed an H^+-to-ATP ratio of 5.9, beyond the highest (5.0) among naturally occurring (one peripheral stalk and single a-subunit) F_1F_O synthases (73). Given the H^+-to-ATP ratio defines the energy cost and the PMF threshold for ATP synthesis, a high H^+-to-ATP ratio lowers the PMF required to overcome the Gibbs free energy of ATP synthesis (ΔG_{ATP}). Considering *C. aurantiacus* grows optimally under normal to alkaline pH conditions with adequate periods of direct sunlight in hot springs (55 to 70 °C) (33), the incorporation of two a-subunits contributes to increase the H^+-to-ATP ratio of CaF_1F_O, enabling ATP synthesis at low or unstable PMF conditions.

Our study of CaF_1F_O provides insights into the structure and proton translocation of ATP synthases from photosynthetic organisms. The unique structural features of CaF_1F_O apparently help to meet the bioenergetic demands under challenging environmental pressures. Regarding applications, the unique architecture of CaF_1F_O immediately suggests potentially innovative strategies for modulating the proton translocation or H^+-to-ATP ratios of engineered ATP synthases and for manipulating photosynthesis in plants or light-driven biomimetic systems and energy metabolism in cells or synthetic organelles. That is, distinct from current efforts based on changing the c-ring stoichiometry, our findings support that researchers can rationally alter the number of a-subunits and/or peripheral stalks to specify distinct outcomes in terms of (for example) proton translocation capacity and enzyme stability. Our results can inspire future structural and mechanistic investigations of ATP synthases from other photosynthetic species, which will reveal whether the features of CaF_1F_O described here are unique to *C. aurantiacus* or are shared by the early photosynthetic organisms.

Materials and Methods

Isolation and Purification of *Ca*F_1F_O from *C. aurantiacus*. Preparation of *C. aurantiacus* membranes and membrane protein solubilization were carried out as described (42). Briefly, *C. aurantiacus* J-10-fl cells were cultured anaerobically at 50 °C under 180 μmol m^{-2} s^{-1} illumination in a modified PE medium for 7 d (33). The cells were harvested by centrifugation at 10,000×*g* for 10 min at 4 °C and were resuspended in buffer containing 50 mM Tris-HCl pH 8.0 (buffer A) before homogenization using a high-pressure homogenizer (Union, China). The cell extracts were centrifuged at 22,000×*g* for 10 min to remove the unbroken cells and insoluble lipids. The whole membrane components were then harvested by centrifugation at 200,000×*g* for 2 h (Ti 70 rotor, 45,000 rpm) at 4 °C.

The membrane pellets were resuspended in buffer A and solubilized by 2% *n*-Dodecyl-β-D-Maltopyranoside (DDM, Anatrace) with gentle stirring at room temperature for 1 h. The solubilized membranes were ultracentrifuged at 200,000×*g* for 1 h at 4 °C. The supernatant was filtered through a 0.22 μm Millipore filter and diluted with four-fold volume of the buffer A. The diluted supernatant was then loaded on a prepacked anion exchange chromatography column (HiTrap Q HP, GE Health) that had been pre-equilibrated with buffer A containing 0.05% DDM (buffer B). The fractions containing CaF_1F_O were eluted from the column with 0.1 M to 0.3 M NaCl in buffer B. The eluents were concentrated using Amicon filters (EMD Millipore), and were further purified using a Uniodex 200 PG 16/60 size-exclusion column (Union, China) in buffer containing 20 mM Tris-HCl pH 8.0, 100 mM NaCl, 0.02% DDM (buffer C). The fractions verified by blue native PAGE and tricine–SDS-PAGE were used for cryo-EM analyses and other experiments.

Cryoelectron Microscopy Grid Preparation and Data Collection. The protein concentration of purified CaF_1F_O was determined by a bicinchoninic acid (BCA) Protein Quantification Kit (Vazyme Biotech Co. Ltd., China). 3 μL of CaF_1F_O at a concentration of 3 mg/mL was applied to freshly glow-discharged GiG R1.2/1.3 300-mesh amorphous alloy film (Zhenjiang Lehua Technology Co. Ltd., China). Each grid was blotted for 3.0 s with a blot force of 1 under 100% humidity at 4 °C, and plunge-frozen in liquid ethane using a Mark IV Vitrobot plunge freezer (Thermo Fisher Scientific, Waltham, MA). To obtain the ADP-bound conformation of CaF_1F_O, the purified CaF_1F_O was incubated with 5 mM $MgCl_2$ and 48 μM ADP before preparing the cryo-EM grids.

Cryo-EM images of the ADP-free and ADP-bound CaF_1F_O were recorded on a 300-kV Titan Krios microscope with a Selectris energy filter and Falcon 4 direct electron detector using EPU software (Thermo Fisher Scientific, USA). A calibrated magnification of 130,000× was used for imaging, corresponding to a pixel size of 0.93 Å. Each movie was dose-fractionated to 40 frames under a total dose rate of 50 $e^-/Å^2$ and an exposure time of 6 s in a defocus range of −0.8 to −1.6 μm. In total, 10,853 movies of ADP-free CaF_1F_O and 10,705 movies of ADP-bound CaF_1F_O were collected. Further details are given in *SI Appendix*, Tables S2 and S3.

Image Processing. Motion correction and contrast transfer function (CTF) estimation were performed using CryoSPARC v3.3.2 (74). For the ADP-free CaF_1F_O dataset, a total of 2,463,962 particles were automatically selected from 10,853 micrographs, extracted, and subjected to two-dimensional (2D) classifications. After several iterations of 2D and three-dimensional (3D) classifications, 443,387 particles were selected and subjected for a new round of 3D classification. These particles were 3D classified into three classes using a 30-Å low-pass–filtered initial model and a full mask. According to the rotational positions of the central stalk relative to the stator, the three classes with unequal particle numbers were assigned as three rotational states of *Ca*F$_1$F$_O$ (231,462 particles in State 1, 169,308 particles in State 2, and 42,617 particles in State 3). Several iterations of heterologous refinement and nonuniform refinement (75) of the particles in each class generated three maps with overall resolutions at 2.84 Å, 2.89 Å, and 3.31 Å, respectively, based on the gold standard Fourier shell correlation (FSC) cut-off of 0.143 (76) (*SI Appendix*, Fig. S3).

To improve the reconstruction of the *Ca*F$_O$ region and the peripheral stalks region, a soft-edged mask around the *Ca*F$_O$, and a mask around *Ca*F$_O$ and the two peripheral stalks were separately applied before local realignment. Focused refinement of the *Ca*F$_O$ regions including a- and c-subunits improved the local resolutions to 3.16, 3.30, and 3.98 Å for each rotational state. Focused refinement including a-, c-, and b-subunits improved the local resolutions of the two peripheral stalks to 3.48, 3.85, and 4.60 Å for each rotational state (*SI Appendix*, Fig. S3*E*).

For the ADP-bound *Ca*F$_1$F$_O$ dataset, a total of 2,452,775 particles were automatically selected from 10,705 micrographs and extracted for 2D classifications. After several iterations of 2D and 3D classifications, 185,010 particles were selected and extracted for a new round of 3D classification, which sorted the particles into three main classes. After several iterations of heterologous refinement and nonuniform refinement of the particles (85,733 particles in State 1, 58,297 particles in State 2, and 37,529 particles in State 3), three final maps were produced with overall resolutions at 2.89 Å, 2.96 Å, and 3.18 Å, respectively, based on the gold standard FSC cut-off of 0.143 (*SI Appendix*, Fig. S4). Focused refinement of the ADP-bound *Ca*F$_1$F$_O$ improved the local resolutions of the *Ca*F$_O$ region to 3.97, 4.10, and 4.28 Å, and the peripheral stalks to 4.08, 4.95, and 5.18 Å for each rotational state (*SI Appendix*, Fig. S4*E*). The values of the angular distribution of particles from 3D refinement were visualized by ChimeraX (60). Local resolution was estimated with Resmap (77).

Model Building and Refinement. The initial model of the ADP-free *Ca*F$_1$F$_O$ was built by fitting *Bacillus PS3* F$_1$F$_O$ (21) (PDB ID: 6N2Y) into the cryo-EM density map in UCSF Chimera (78). Based on the density map, the atomic model of the ADP-free *Ca*F$_1$F$_O$, including the amino acid residues and cofactors, was manually built, and adjusted in Coot (79). Then real-space refinement in PHENIX (80) was used for model refinement, using the Ramachandran restraints followed by manual rebuilding in Coot. The structure of the ADP-bound *Ca*F$_1$F$_O$ was manually built using the refined model of ADP-free *Ca*F$_1$F$_O$ as a reference in Coot and was refined using the real-space refinement in PHENIX. The refinement statistics are summarized in *SI Appendix*, Tables S2 and S3. All figures were drawn in PyMOL (The PyMOL Molecular Graphics System, Version 2.5.2, Schrödinger, LLC.), UCSF Chimera, and ChimeraX.

Reconstitution of *Ca*F$_1$F$_O$ into Proteoliposomes. The purified *Ca*F$_1$F$_O$ was separately reconstituted into proteoliposomes using a modification of the previously described methods (81). 25 mg of phosphatidylcholine (Sigma-Aldrich) was suspended in 1 mL of lipid-solubilization buffer containing10 mM Tricine-KOH (pH 8.0), 2 mM MgCl$_2$, and 1 mM dithiothreitol. The suspension was sonicated twice for 1 min (150 W, Scientz JY92-IIN, China) and cooled on ice for 1 h, and was then mixed with 0.25 mg of *Ca*F$_1$F$_O$ in a lipid-to-protein ratio of 50:1 (wt/wt). To facilitate insertion of *Ca*F$_1$F$_O$ into the liposomes, 0.8% Triton X-100 was added to the mixture, which was cooled down on ice for 20 min before being gently stirred at room temperature for 45 min. Then three aliquots of Bio-Beads SM-2 (Bio-Rad) (80, 80, and 100 mg) were added to the mixture at time intervals of 90-, 90-, and 30-min to remove the included Triton X-100. After Bio-Bead removal by centrifugal filtration, the reconstituted *Ca*F$_1$F$_O$ proteoliposomes were immediately used for the ATP synthesis and hydrolysis activity assays.

ATP Synthesis Activity. The ATP synthesis activity of the reconstructed *Ca*F$_1$F$_O$ proteoliposomes was separately determined using the luciferase-luciferin system as previously described (81). The reaction was monitored using an ATP Assay Kit (Beyotime Biotechnology, China). Briefly, 20 μL proteoliposomes were mixed with 80 μL acidic buffer comprising 50 mM succinate (pH 4.5), 5 mM NaH$_2$PO$_4$, 2 mM MgCl$_2$, 0.5 mM ADP, 150 mM KCl, and 2 μM valinomycin (freshly added). The mixture was incubated at room temperature for 5 min, to keep high proton concentrations inside the proteoliposomes. Then 20 μL of the treated proteoliposomes was added into the reaction mixture (180 μL) containing 100 mM Tricine-KOH (pH 8.5), 5 mM NaH$_2$PO$_4$, 2 mM MgCl$_2$, 0.5 mM ADP, 150 mM KCl, 2 μM valinomycin (freshly added), and 20 μL luciferin/luciferase reagent. Instantly, the luminescence generated from the reaction was recorded by a multimode microplate reader (TECAN Spark, Switzerland) equipped with a luminometer. Production of ATP during the reaction was calculated from a standard curve, in which the luminescence was plotted against the ATP concentration. All data were obtained from three replicative experiments, with the mean and SD calculated and plotted.

ATP Hydrolysis Activity. The ATP hydrolysis activity of *Ca*F$_1$F$_O$ was measured as previously described (82). *Ca*F$_1$F$_O$ catalyzed ADP hydrolysis was coupled to pyruvate kinase (PK) that transfers a phosphate group from phosphoenolpyruvate (PEP) to ADP for pyruvate generation, and lactate dehydrogenase (LDH) that catalyzes the NADH-dependent conversion of pyruvate to lactate. The reaction mixture contains 50 mM Tris-HCl (pH 8.0), 150 mM NaCl, 2 mM MgCl$_2$, 0.1 mM NADH, 1.5 mM phosphoenolpyruvate, 3.2 units PK, 4 units LDH, 0.04% DDM, 0.1 mg/mL *Ca*F$_1$F$_O$. The reaction was initiated by addition of 1 mM ATP, then the absorbance of NADH at 340 nm was recorded by a UV–vis spectrophotometer (Mapada P6, China) for 120 s at 37 °C. All enzymatic data were obtained from triplicate experiments.

Data, Materials, and Software Availability. Cryo-EM maps and atomic models data have been deposited in Electron Microscopy Data Bank (EMDB) (83) and Protein Data Bank (PDB) (84) (Cryo-EM maps have been deposited in the EMDB under the following accession numbers: EMD-60868, EMD-60869, EMD-60870, EMD-60871, EMD-60872, EMD-60873, EMD-60874, EMD-60875, EMD-60876, EMD-60877, EMD-60878, EMD-60879, EMD-60880, EMD-60881, EMD-60882, EMD-60883, EMD-60884, and EMD-60885. Atomic models have been deposited in the PDB under the following accession numbers PBD ID: 9ITJ, 9ITK, 9ITL, 9ITM, 9ITN, 9ITO, 9ITP, 9ITQ, 9ITR, 9ITS, 9ITT, 9ITU, 9ITV, 9ITW, 9ITX, 9ITY, 9ITZ, and 9IU0.). All study data are included in the article and/or supporting information.

ACKNOWLEDGMENTS. We thank Professor Fei Sun at Institute of Biophysics, Chinese Academy of Sciences for helpful discussions. We thank Professors Robert E. Blankenship at Washington University and Yueyong Xin at Hangzhou Normal University for providing the *Chloroflexus aurantiacus* J-10-fl cells.We also thank Dr. Shenghai Chang in the Center of Cryo-Electron Microscopy (CCEM), Zhejiang University for his technical assistance on Cryo-EM data collection. The image processing, model building, and structural and biochemical studies were performed at Hangzhou Normal University.Funding was provided by National Natural Science Foundation of China (32471270, 32171227, 31870740), Zhejiang Provincial Natural Science Foundation of China (LR22C020002) and Interdisciplinary Research Project of Hangzhou Normal University (2024JCXK04) to X.L.X.

Author affiliations: [a]Zhejiang Key Laboratory of Medical Epigenetics, Department of Biochemistry and Molecular Biology, School of Basic Medical Sciences, Hangzhou Normal University, Hangzhou 311121, China; [b]Photosynthesis Research Center, College of Life and Environmental Sciences, Hangzhou Normal University, Hangzhou 311121, China; and [c]Laboratory of Structural Biology, School of Medicine, Tsinghua University, Beijing 100084, China

1. P. Mitchell, Coupling of phosphorylation to electron and hydrogen transfer by a chemi-osmotic type of mechanism. *Nature* **191**, 144–148 (1961).
2. S. R. Ketcham, J. W. Davenport, K. Warncke, R. E. McCarty, Role of the gamma subunit of chloroplast coupling factor 1 in the light-dependent activation of photophosphorylation and ATPase activity by dithiothreitol. *J. Biol. Chem.* **259**, 7286–7293 (1984).
3. W. Kuhlbrandt, Structure and mechanisms of F-Type ATP synthases. *Annu. Rev. Biochem.* **88**, 515–549 (2019).
4. J. P. Abrahams, A. G. Leslie, R. Lutter, J. E. Walker, Structure at 2.8 A resolution of F1-ATPase from bovine heart mitochondria. *Nature* **370**, 621–628 (1994).
5. D. Stock, A. G. Leslie, J. E. Walker, Molecular architecture of the rotary motor in ATP synthase. *Science* **286**, 1700–1705 (1999).
6. A. Cheuk, T. Meier, Rotor subunits adaptations in ATP synthases from photosynthetic organisms. *Biochem. Soc. Trans.* **49**, 541–550 (2021).
7. H. Guo, J. L. Rubinstein, Cryo-EM of ATP synthases. *Curr. Opin. Struct. Biol.* **52**, 71–79 (2018).
8. A. Hahn, J. Vonck, D. J. Mills, T. Meier, W. Kuhlbrandt, Structure, mechanism, and regulation of the chloroplast ATP synthase. *Science* **360**, eaat4318 (2018).
9. H. S. Van Walraven, R. Lutter, J. E. Walker, Organization and sequences of genes for the subunits of ATP synthase in the thermophilic cyanobacterium Synechococcus 6716. *Biochem. J.* **294**, 239–251 (1993).
10. R. Borghese, P. Turina, L. Lambertini, B. A. Melandri, The atpIBEXF operon coding for the F0 sector of the ATP synthase from the purple nonsulfur photosynthetic bacterium Rhodobacter capsulatus. *Arch Microbiol.* **170**, 385–388 (1998).

11. G. Falk, A. Hampe, J. E. Walker, Nucleotide sequence of the Rhodospirillum rubrum atp operon. *Biochem. J.* **228**, 391–407 (1985).
12. G. Falk, J. E. Walker, Transcription of Rhodospirillum rubrum atp operon. *Biochem. J.* **229**, 663–668 (1985).
13. A. L. Cozens, J. E. Walker, The organization and sequence of the genes for ATP synthase subunits in the cyanobacterium Synechococcus 6301. Support for an endosymbiotic origin of chloroplasts. *J. Mol. Biol.* **194**, 359–383 (1987).
14. G. Falk, J. E. Walker, DNA sequence of a gene cluster coding for subunits of the F0 membrane sector of ATP synthase in Rhodospirillum rubrum. Support for modular evolution of the F1 and F0 sectors. *Biochem. J.* **254**, 109–122 (1988).
15. A. P. Srivastava *et al.*, High-resolution cryo-EM analysis of the yeast ATP synthase in a lipid membrane. *Science* **360**, eaas9699 (2018).
16. J. Gu *et al.*, Cryo-EM structure of the mammalian ATP synthase tetramer bound with inhibitory protein IF1. *Science* **364**, 1068–1075 (2019).
17. S. B. Vik, B. J. Antonio, A mechanism of proton translocation by F1F0 ATP synthases suggested by double mutants of the a subunit. *J. Biol. Chem.* **269**, 30364–30369 (1994).
18. I. N. Watt, M. G. Montgomery, M. J. Runswick, A. G. Leslie, J. E. Walker, Bioenergetic cost of making an adenosine triphosphate molecule in animal mitochondria. *Proc. Natl. Acad. Sci. U.S.A.* **107**, 16823–16827 (2010).
19. Y. Lai *et al.*, Structure of the human ATP synthase. *Mol Cell* **83**, 2137–2147.e2134 (2023).
20. H. Guo *et al.*, Structure of mycobacterial ATP synthase bound to the tuberculosis drug bedaquiline. *Nature* **589**, 143–147 (2021).
21. H. Guo, T. Suzuki, J. L. Rubinstein, Structure of a bacterial ATP synthase. *Elife* **8**, e43128 (2019).
22. D. Matthies *et al.*, High-resolution structure and mechanism of an F/V-hybrid rotor ring in a Na(+)-coupled ATP synthase. *Nat. Commun.* **5**, 5286 (2014).
23. L. Preiss *et al.*, The c-ring stoichiometry of ATP synthase is adapted to cell physiological requirements of alkaliphilic Bacillus pseudofirmus OF4. *Proc. Natl. Acad. Sci. U.S.A.* **110**, 7874–7879 (2013).
24. L. Preiss *et al.*, The c-ring ion binding site of the ATP synthase from Bacillus pseudofirmus OF4 is adapted to alkaliphilic lifestyle. *Mol. Microbiol.* **92**, 973–984 (2014).
25. D. Pogoryelov *et al.*, The oligomeric state of c rings from cyanobacterial F-ATP synthases varies from 13 to 15. *J. Bacteriol.* **189**, 5895–5902 (2007).
26. G. A. Davis, D. M. Kramer, Optimization of ATP synthase c-rings for oxygenic photosynthesis. *Front Plant Sci.* **10**, 1778 (2019).
27. T. Ruhle, D. Leister, V. Pasch, Chloroplast ATP synthase: From structure to engineering. *Plant Cell* **36**, 3974–3996 (2024), 10.1093/plcell/koae081.
28. J. H. Yang, D. Williams, E. Kandiah, P. Fromme, P. L. Chiu, Structural basis of redox modulation on chloroplast ATP synthase. *Commun. Biol.* **3**, 482 (2020).
29. S. Murakami *et al.*, Structure of the γ-ε complex of cyanobacterial F(1)-ATPase reveals a suppression mechanism of the γ subunit on ATP hydrolysis in phototrophs. *Biochem. J.* **475**, 2925–2939 (2018).
30. Y. Jia, J. Li, Reconstitution of FoF1-ATPase-based biomimetic systems. *Nat. Rev. Chem.* **3**, 361–374 (2019).
31. P. J. Harris, M. M. Burrell, M. J. Emes, I. J. Tetlow, Effects of post-anthesis high-temperature stress on carbon partitioning and starch biosynthesis in a spring wheat (Triticum aestivum L.) adapted to moderate growth temperatures. *Plant Cell Physiol.* **64**, 729–745 (2023).
32. K. Y. Lee *et al.*, Photosynthetic artificial organelles sustain and control ATP-dependent reactions in a protocellular system. *Nat. Biotechnol.* **36**, 530–535 (2018).
33. B. K. Pierson, R. W. Castenholz, A phototrophic gliding filamentous bacterium of hot springs, Chloroflexus aurantiacus, gen. and sp. nov. *Arch Microbiol.* **100**, 5–24 (1974).
34. S. Hanada, B. K. Pierson "The family chloroflexaceae" in *The Prokaryotes*. (2006), 10.1007/0-387-30747-8_33, Chapter 33, pp. 815–842.
35. Y. Xin *et al.*, Cryo-EM structure of the RC-LH core complex from an early branching photosynthetic prokaryote. *Nat. Commun.* **9**, 1568 (2018).
36. J. Xin *et al.*, Carotenoid assembly regulates quinone diffusion and the Roseiflexus castenholzii reaction center-light harvesting complex architecture. *Elife* **12**, e88951 (2023).
37. Y. Shi *et al.*, Cryo-EM structures of the air-oxidized and dithionite-reduced photosynthetic alternative complex III from Roseiflexus castenholzii. *Sci. Adv.* **6**, eaba2739 (2020).
38. J. Xin *et al.*, Cryo-EM structure of HQNO-bound Alternative Complex III from the anoxygenic phototrophic bacterium Chloroflexus aurantiacus. *Plant Cell* **36**, 4212–4233 (2024), 10.1093/plcell/koae029.
39. C. Wang *et al.*, Structural basis underlying the electron transfer features of a blue copper protein auracyanin from the photosynthetic bacterium Roseiflexus castenholzii. *Photosynth Res.* **143**, 301–314 (2020).
40. L. Yu *et al.*, A cytochrome c(551) mediates the cyclic electron transport chain of the anoxygenic phototrophic bacterium Roseiflexus castenholzii. *Plant Commun.* **5**, 100715 (2024).
41. K. H. Tang *et al.*, Complete genome sequence of the filamentous anoxygenic phototrophic bacterium Chloroflexus aurantiacus. *BMC Genomics* **12**, 334 (2011).
42. M. F. Yanyushin, Subunit structure of ATP synthase from Chloroflexus aurantiacus. *FEBS Lett.* **335**, 85–88 (1993).
43. L. Zhou, L. A. Sazanov, Structure and conformational plasticity of the intact Thermus thermophilus V/A-type ATPase. *Science* **365**, eaaw9144 (2019).
44. M. Sobti *et al.*, Cryo-EM structures provide insight into how E. coli F(1)F(o) ATP synthase accommodates symmetry mismatch. *Nat. Commun.* **11**, 2615 (2020).
45. A. Zhou *et al.*, Structure and conformational states of the bovine mitochondrial ATP synthase by cryo-EM. *Elife* **4**, e10180 (2015).
46. P. D. Boyer *et al.*, Oxidative phosphorylation and photophosphorylation. *Annu. Rev. Biochem.* **46**, 955–966 (1977).
47. M. Sobti *et al.*, Changes within the central stalk of E. coli F(1)F(o) ATP synthase observed after addition of ATP. *Commun. Biol.* **6**, 26 (2023).
48. M. Sobti *et al.*, Cryo-EM structures of the autoinhibited E. coli ATP synthase in three rotational states. *Elife* **5**, e21598 (2016).
49. M. Sobti *et al.*, Cryo-EM reveals distinct conformations of E. coli ATP synthase on exposure to ATP. *Elife* **8**, e43864 (2019).
50. J. K. Demmer *et al.*, Structure of ATP synthase from ESKAPE pathogen Acinetobacter baumannii. *Sci. Adv.* **8**, eabl5966 (2022).
51. E. Morales-Rios, M. G. Montgomery, A. G. Leslie, J. E. Walker, Structure of ATP synthase from Paracoccus denitrificans determined by X-ray crystallography at 4.0 A resolution. *Proc. Natl. Acad. Sci. U.S.A.* **112**, 13231–13236 (2015).
52. A. P. Srivastava *et al.*, High-resolution cryo-EM analysis of the yeast ATP synthase in a lipid membrane. *Science* **360**, eaas9699 (2018).
53. B. J. Murphy *et al.*, Rotary substates of mitochondrial ATP synthase reveal the basis of flexible F(1)-F(o) coupling. *Science* **364**, eaaw9128 (2019).
54. G. Pinke, L. Zhou, L. A. Sazanov, Cryo-EM structure of the entire mammalian F-type ATP synthase. *Nat. Struct. Mol. Biol.* **27**, 1077–1085 (2020).
55. T. E. Spikes, M. G. Montgomery, J. E. Walker, Structure of the dimeric ATP synthase from bovine mitochondria. *Proc. Natl. Acad. Sci. U.S.A.* **117**, 23519–23526 (2020).
56. G. M. Courbon *et al.*, Mechanism of mycobacterial ATP synthase inhibition by squaramides and second generation diarylquinolines. *EMBO J.* **42**, e113687 (2023).
57. Y. Zhang *et al.*, Inhibition of M. tuberculosis and human ATP synthase by BDQ and TBAJ-587. *Nature* **631**, 409–414 (2024).
58. M. Allegretti *et al.*, Horizontal membrane-intrinsic α-helices in the stator a-subunit of an F-type ATP synthase. *Nature* **521**, 237–240 (2015).
59. A. Nakano, J. I. Kishikawa, K. Mitsuoka, K. Yokoyama, Mechanism of ATP hydrolysis dependent rotation of bacterial ATP synthase. *Nat. Commun.* **14**, 4090 (2023).
60. E. F. Pettersen *et al.*, UCSF ChimeraX: Structure visualization for researchers, educators, and developers. *Protein Sci* **30**, 70–82 (2021).
61. C. M. Nalin, R. E. McCarty, Role of a disulfide bond in the gamma subunit in activation of the ATPase of chloroplast coupling factor 1. *J. Biol. Chem.* **259**, 7275–7280 (1984).
62. M. Toei, H. Noji, Single-molecule analysis of F0F1-ATP synthase inhibited by N,N-dicyclohexylcarbodiimide. *J. Biol. Chem.* **288**, 25717–25726 (2013).
63. D. Pogoryelov *et al.*, Microscopic rotary mechanism of ion translocation in the F(o) complex of ATP synthases. *Nat. Chem. Biol.* **6**, 891–899 (2010).
64. W. Zhou, J. D. Faraldo-Gomez, Membrane plasticity facilitates recognition of the inhibitor oligomycin by the mitochondrial ATP synthase rotor. *Biochim. Biophys. Acta Bioenerg.* **1859**, 789–796 (2018).
65. L. Wang, D. Wu, C. V. Robinson, H. Wu, T. M. Fu, Structures of a complete human V-ATPase reveal mechanisms of its assembly. *Mol. Cell* **80**, 501–511 e503 (2020).
66. Y. M. Abbas, D. Wu, S. A. Bueler, C. V. Robinson, J. L. Rubinstein, Structure of V-ATPase from the mammalian brain. *Science* **367**, 1240–1246 (2020).
67. R. Wang *et al.*, Cryo-EM structures of intact V-ATPase from bovine brain. *Nat. Commun.* **11**, 3921 (2020).
68. C. Wang *et al.*, Structure and topography of the synaptic V-ATPase-synaptophysin complex. *Nature* **631**, 899–904 (2024), 10.1038/s41586-024-07610-x.
69. C. E. Coupland *et al.*, High-resolution electron cryomicroscopy of V-ATPase in native synaptic vesicles. *Science* **385**, 168–174 (2024), 10.1126/science.adp5577.
70. Y. Z. Tan *et al.*, CryoEM of endogenous mammalian V-ATPase interacting with the TLDc protein mEAK-7. *Life Sci. Alliance* **5**, e202201527 (2022).
71. T. Vasanthakumar *et al.*, Structural comparison of the vacuolar and Golgi V-ATPases from Saccharomyces cerevisiae. *Proc. Natl. Acad. Sci. U.S.A.* **116**, 7272–7277 (2019).
72. Y. Z. Tan *et al.*, Structure of V-ATPase from citrus fruit. *Structure* **30**, 1403–1410.e1404 (2022).
73. H. Ueno *et al.*, Engineering of ATP synthase for enhancement of proton-to-ATP ratio. bioRxiv [Preprint] (2024), https://doi.org/10.1101/2024.08.27.60990 (Accessed 27 August 2024).
74. A. Punjani, J. L. Rubinstein, D. J. Fleet, M. A. Brubaker, cryoSPARC: Algorithms for rapid unsupervised cryo-EM structure determination. *Nat. Methods* **14**, 290–296 (2017).
75. A. Punjani, H. Zhang, D. J. Fleet, Non-uniform refinement: Adaptive regularization improves single-particle cryo-EM reconstruction. *Nat. Methods* **17**, 1214–1221 (2020).
76. M. van Heel, M. Schatz, Fourier shell correlation threshold criteria. *J. Struct. Biol.* **151**, 250–262 (2005).
77. A. Kucukelbir, F. J. Sigworth, H. D. Tagare, Quantifying the local resolution of cryo-EM density maps. *Nat. Methods* **11**, 63–65 (2014).
78. T. D. Goddard, C. C. Huang, T. E. Ferrin, Visualizing density maps with UCSF Chimera. *J. Struct. Biol.* **157**, 281–287 (2007).
79. P. Emsley, K. Cowtan, Coot: Model-building tools for molecular graphics. *Acta Crystallogr. D Biol. Crystallogr.* **60**, 2126–2132 (2004).
80. P. D. Adams *et al.*, PHENIX: A comprehensive Python-based system for macromolecular structure solution. *Acta Crystallogr. D Biol. Crystallogr.* **66**, 213–221 (2010).
81. S. Fischer, P. Gräber, Comparison of ΔpH- and Δφ φ-driven ATP synthesis catalyzed by the H+-ATPases from Escherichia coli or chloroplasts reconstituted into liposomes *FEBS Lett.* **457**, 327–332 (1999).
82. G. M. Cook *et al.*, Purification and biochemical characterization of the F1Fo-ATP synthase from thermoalkaliphilic Bacillus sp. strain TA2.A1. *J. Bacteriol.* **185**, 4442–4449 (2003).
83. European Bioinformatics Institute (EBI), Electron Microscopy Data Bank (EMDB). https://www.ebi.ac.uk/pdbe/emdb. Accessed 12 March 2025.
84. Research Collaboratory for Structural Bioinformatics (RCSB), Protein Data Bank (PDB). https://www.rcsb.org. Accessed 12 March 2025.